JOURNAL OF SOLID STATE CHEMISTRY 109, 359–371 (1994)

# Scanning Tunneling Microscopy and Crystal Chemical Models of the $Na_{0.82}WO_3$ (001) Surface

Gregory S. Rohrer,[1] Weier Lu, Michael L. Norton,* Michael A. Blake,* and Cathy Lane Rohrer†

*Department of Materials Science and Engineering, Carnegie Mellon University, Pittsburgh, Pennsylvania 15213; *Department of Chemistry, Marshall University, Huntington, West Virginia 25701; and †Aluminum Company of America, Alcoa Technical Center, Alcoa Center, Pennsylvania 15069-0001*

Received June 21, 1993; accepted September 1, 1993

The cleaved (001) surface of $Na_{0.82}WO_3$, a cubic tungsten bronze, has been imaged with a scanning tunneling microscope. The periodicity of the atomic-scale contrast in these images can be described by a rectangular cell with $a$ equal to the bulk lattice parameter and $b = 2a$. A crystal chemical model for the surface structure, based on the bond valence and distance-least-squares methods, has been used to show that an ordered distribution of Na in the near surface region could lead to atomic relaxations and the observed $1 \times 2$ structure. Based on the atomic positions predicted by this model, constant current STM images have been calculated for a variety of parameters. The experimental observations are consistent with simulated images of the W–O terminated surface. 

## INTRODUCTION

$Na_{0.82}WO_3$ belongs to the family of nonstoichiometric cubic tungsten bronzes (CTB) with the general formula $A_xWO_3$. The CTB phases crystallize in the $ABO_3$ perovskite structure with incomplete occupation of the $A$ site. The manner in which the bulk structural (1), electrical (2–5), superconducting (6), and magnetic (7, 8) properties are related to the composition ($x$) has been established by extensive research.

The stoichiometric versatility of this system, together with its well-known bulk properties, provides an opportunity to examine the manner in which the surface composition, structure, and properties are related to those of the bulk. This opportunity has been exploited by many researchers who have studied the surface reactivity (9–11), surface structure (12–15), and surface electronic structure (16–21) as a function of composition. While it would be desirable to relate known changes in surface properties, such as reactivity, to changes in the surface structure, the structural data are limited to knowledge of the surface cell periodicity. The structural features that have yet to be described include the atomic termination layer, the relative positions of surface atoms, and the characteristic nonperiodic elements of the structure.

The present paper describes efforts to determine these details of the atomic-scale surface structure using scanning tunneling microscopy (STM). The ability of the tunneling microscope to record real-space, atomic-scale resolution images of metal oxide surfaces has been clearly demonstrated in recent publications (22–25). However, experience shows that interpreting STM images from complex binary or ternary oxide surfaces can be considerably more challenging than recording the observations. The problem is somewhat simplified for the surfaces of two-dimensional materials that are formed by cleavage at a van der Waals gap. In this case, the surfaces are unreconstructed and STM images can be interpreted in terms of bulk crystallographic data. STM observations from the surfaces of cleaved three-dimensionally bonded compounds, however, are typically interpreted only on the basis of qualitative arguments. Among the barriers to more quantitative interpretations are the multiple termination layer possibilities, the inability to form images from both the bonding and antibonding bands (due to their large energy separation), uncertainties with respect to the electronic structure of the surface, and ill-defined tip structures.

In this paper we describe both the atomic-scale STM imaging of the $Na_{0.82}WO_3$ (100) surface and the models that we have used to interpret the observations. The atomistic models for different possible surface terminations are generated by the quantitative application of crystal chemical empiricisms within the framework of the bond-valence and distance-least-squares (BV/DLS) methods. These methods, based on Pauling's rules (26) and the vast amount of structural data in the crystallographic data base, have been developed over the last decade by Brown

[1] To whom correspondence should be addressed. E-mail: gr20@andrew.cmu.edu.



0022-4596/94 $6.00

(27) and O'Keeffe (28) and have been successfully used to model bulk structures (22–29). More recently, these methods have been used to describe the relaxation around defects (30) and interfaces (31), and in this paper we apply them to a free surface. Using the atomic positions predicted by the crystal chemical model, the tunneling current is calculated as a function of lateral and vertical position above the surface using a simplified tunneling model. The results of the tunneling current calculations are then used to construct constant current images that can be compared to the experimental observations. By calculating simulated images for the limiting cases of different termination layers, different tip sizes, and different electronic structures, it is possible to systematically explore the important parameters and choose a model that most closely matches the experimental observations.

## EXPERIMENTAL PROCEDURE

### *(a) Crystal Growth*

Single crystals of the CTB were grown using a fused salt electrolysis method similar to that described by Shanks (32). A target composition of $Na_{0.85}WO_3$ was chosen for both chemical and thermal reasons. Chemically, this composition is near the center of the metallic phase field, minimizing the probability that crystal size and perfection would be limited by the nucleation and growth of secondary phases. At the same time, the proximity of this composition to the low melting eutectic maximizes the range of useful melt temperatures. This condition allows crystals to be grown at the relatively low temperature of 750°C, while being far enough (100°C) above the liquidus to suppress secondary nucleation due to impurities or clusters in the melt.

Shanks's results suggest that a 25-mole% solution of $Na_2WO_4$ in $WO_3$ should be used to grow the targeted composition. Rather than using the starting materials suggested by Shanks, an equivalent solution was formed from the reaction of 153.8 g (0.6155 mole) of orthotungstic acid and 49.94 g (0.4617 mole) of sodium carbonate, both of technical grade. A slow bubbling was observed in the clear viscous melt and attributed to prolonged carbon dioxide evolution from the reaction of the starting materials. For a typical run, the temperature was stalled at 700°C for 4 hr to allow relative completion of this gas generating reaction.

A two-electrode cell with an inert gas atmosphere was used. It consisted of an alundum crucible (Coors) contained in a quartz envelope through which dry nitrogen could be passed. The jointed top of the quartz envelope also allowed observation of the melt and introduction and positioning of the two electrodes. The cell assembly was contained in and heated by a single zone vertical tube furnace. After reaching the growth temperature of 750°C, the electrodes (1-mm-diameter platinum anode and 1-mm-diameter silver cathode [Aesar], approximate length 0.75 cm for each) were inserted into the melt, and a constant current of 20 mA applied. A cluster of bright red metallic crystals weighing approximately 8.7 g was harvested by quenching after 43 hr. The crystals, which quickly changed to a golden brown metallic color upon exposure to air, displayed the expected cubic morphology, with many {100} facets approaching 2 × 2 mm in size. Adherent flux material was dissolved in hot distilled water.

Pieces of the crystal that remained after cleavage (those not used for STM analysis) were pulverized for powder X-ray diffraction analysis. The cubic lattice constant, $a = 3.8521(2)$ Å, was determined from a least-squares refinement of 16 well-measured peaks. Using the well-known relationship between the lattice parameter and the Na composition, it was determined that the value for $x$ in the $Na_xWO_3$ crystal studied was 0.82 (33). It should be noted that the X-ray diffraction analysis suggested that the single crystals were not entirely uniform; Laue patterns indicated that some samples had low angle grain boundaries, and inhomogeneous broadening of the higher angle diffraction peaks in the powder pattern suggested compositional variations.

### *(b) Imaging*

Fresh {001} surfaces were formed by cleavage in air immediately before insertion into the vacuum chamber which had a base pressure of less than $1 \times 10^{-9}$ Torr. Samples were imaged either in the "as cleaved" condition, with no further treatment, or after annealing for 5 hr at 500°C in $6 \times 10^{-8}$ Torr oxygen, a process that has been reported to clean the surface (12). The tips used in these experiments were formed by clipping Pt-10% Ir wire. All of the images were acquired in the constant current mode using a 0.4 V sample bias (tunneling to unoccupied sample states) and a tunnel current of ~1.0 nA. Attempts to form images by tunneling from valence band states were unsuccessful. Similar atomic-scale observations were produced from 3 different samples and characteristic images are presented in the next section. The images are presented in a gray scale in which the white-to-black contrast represents the top-to-bottom vertical height variation. The contrast scales on each image are adjusted to optimize the visual effect and a digital filter was used to remove high frequency noise.

### *(c) Computing Atomic Positions Using BV/DLS*

Complete descriptions of the BV/DLS methods can be found in the literature (27, 28, 34, 35). However, a brief description is given here which emphasizes the application of this method to free surfaces. Pauling's electrostatic

bond valence principle states that with each bond in a solid there is an associated bond valence, $s_{ij}$, between atoms $i$ and $j$ and that the bond valences around each atom sum to its formal valence (26). In general, however, this valence sum rule does not provide enough constraints to determine all of the bond valences in a crystal structure. Additional constraints are found in the rule proposed by Brown (34) which states that bonds between similar pairs of atoms will be as nearly equal as possible. The quantitative application of "Brown's rule" constrains the sum of bond valences around any loop in the crystal structure (taken with alternating signs) to be zero. The proper application of the valence sum rule and Brown's rule allows the formulation of an independent set of linear equations which can be solved simultaneously to give the valence of each bond in a crystal (35).

Structural information is derived from the bond valences through the empirical relationship

$$d_{ij} = R_{ij} - 0.37 \ln(S_{ij})$$

In this expression, $d_{ij}$ is the length of the bond between atoms $i$ and $j$ and $R_{ij}$ is the empirical "bond-valence parameter." The bond-valence parameters for specific atom pairs have been determined from information in the crystallographic data base (36). The data for the calculation are chosen from structures in which the ligands surrounding a cation are identical and there is no disorder. The values derived from 10 to 20 cation environments (or more) are averaged, resulting in values of $R_{ij}$ which typically have standard deviations of less than 0.01 Å. The values $R_{ij}$ used in this work were taken from reference (36) and are given in Table 1.

While bond distances alone contain enough information to specify a crystal structure, it is often more useful to have atomic coordinates. Therefore, the DLS method of Meier and Villiger (37) is used to refine atomic coordinates which best fit the predicted bond lengths. In this procedure, the function

$$R_i = \sum_{j=1,n} w_{ij}^2 [d_{ij}(x, y, z) - d_{ij}^0]^2$$

is minimized, where $n$ is the number of bonds, $d_{ij}^0$ is the target bond length predicted from the bond-valence calculation, $d_{ij}(x, y, z)$ is the bond length calculated from trial atomic coordinates and $w_{ij}$ is a weighting parameter. Baur (38) has pointed out that this procedure is mathematically the same as minimizing the total potential energy of a system of elastic springs where, by analogy, each bond is a spring, $d_{ij}^0$ is the equilibrium length of the spring and $w_{ij}$ is the spring constant. In this work, all bonds were given uniform weight.

TABLE 1
**Parameters for the Bond Valence Model of $Na_{3/4}WO_3$**

| | |
|---|---|
| Lattice constant | 3.852 Å |
| $R_{ij}$, W–O[a] | 1.917 Å |
| $R_{ij}$, Na–O[a] | 1.803 Å |
| Ideal[b] W valence sum | 5.86 |
| Ideal Na valence sum | 1.00 |
| Ideal O valence sum | 2.20 |
| Ideal W–O bond length | 1.926 Å |
| Ideal Na–O bond length | 2.724 Å |

[a] From Ref. (36).
[b] The "ideal" numbers are based on the X-ray determined lattice parameter.

Using the BV/DLS methods to model free surfaces rather than bulk structures requires several modifications. First, since the bulk structure is well known, we assign to each atom a valence based on the known bond lengths so that in the bulk limit the method exactly reproduces the correct structure. Using the X-ray diffraction determined lattice parameter, we find that the sum at the Na site is exactly 1.0, as expected, but that the sums at the O and W sites are 2.2 and 5.86, respectively. This choice of valences is largely a matter of convenience to produce a result with the observed unit cell size; the results of calculations using "formal" valences (W = 5.25, Na = 1, O = 2) were not significantly different.

Second, the loss of translational symmetry that accompanies surface formation requires the choice of a model of finite size terminated on one side by a free surface (with under-coordinated atoms) and on the other by the bulk. Our model uses nine layers of atoms, with the lower atoms fixed at bulk crystallographic positions.

Third, the loss of translational symmetry normal to the surface creates a condition in which the set of equations used to determine the valence of each bond is not unique. In a system of $N$ atoms with three-dimensional translational periodicity, there are only $N-1$ independent valence sums (35). However, in the finite systems examined here, the valence sum at each site is independent. For each of our models, the total number of independent valence sums and loop equations exceeds the number of unknown bonds ($\nu$) and thus, the choice of equations is not unique. We found that satisfactory solutions were obtained when $N-1$ valence sums were augmented with $\nu-N-1$ loop equations. In each case, we omitted the atom in which the valence sum was most greatly reduced by surface creation. The rationale is that this is the atom least likely to fully compensate the lost valence through bond shortening relaxations and thus should not be constrained to bulk values. In each case, the resultant sum at the unconstrained site was intermediate between the

valence at an unrelaxed surface site and the valence at a bulk site.

The final modification is that in the DLS determination of atomic positions, we have allowed relaxations based on the point symmetry of the atom in the bulk structure, plus relaxation perpendicular to the free surface.

*(d) Computing Constant Current Images*

After computing the atomic positions with the BV/DLS model, the tunneling current was calculated as a function of the tip's lateral and vertical position over the sample by assuming that each atom in the model contributes independently to the tunneling current and that at any specific coordinate, the tunneling current is given by a superposition of these contributions:

$$I = \sum_i D_i \exp(-1.025\, S_i \sqrt{\phi}).$$

For the tunnel barrier height, $\phi$, we used the value of 1.6 eV, which was determined from an experimental measurement of the dependence of $I$ on $S_i$. $S_i$ is defined as the distance between the surface of the tip (a sphere with radius $r_{tip}$) and the surface of the $i$th atom, which is a hard sphere the size of which is defined by the ionic radius. Although not explicitly in the equation for the tunneling current, the tip radius influences the current through its effect on the separations, $S_i$. $D_i$ is the relative contribution of the $i$th atom to the total density of electronic states in the conduction band (the band being probed in the STM images). This term is meant to represent, in the simplest possible way, the lateral variation of the surface density of states. For example, for a surface terminated by a single element, all $D_i$ would be equal. For a binary surface layer, on the other hand, we would expect the density of conduction band states to be higher at the electropositive element and would weight the values of $D_i$ appropriately. Once the current is determined at each position, constant current images can be easily extracted.

While we realize that this model is naive, we also believe that the success of a more sophisticated model would be limited by a number of ill-defined parameters including the tip structure, the tip chemistry, and the surface bonding. Therefore, instead of attempting a definitive calculation, we use a computationally simple model which allows a variety of parameters to be explored within reasonable limits. While we do not expect quantitative accuracy from these simulations, they do provide tangible manifestations of the often-used qualitative arguments based on the convolution of geometric and electronic effects, and they are thus useful to support interpretations.

The parameters that were found to have the most significant effect on the images are the relative contribution of the atoms to the conduction band density of states ($D_i$) and the tip size ($r_{tip}$); choice of the constant current level or the barrier height influence only the total vertical corrugation and do not substantially alter the appearance of the image or the shapes of features, since images are normalized to maximize contrast. For the two different termination models, we computed images using an infinitely small tip, a tip the size of a Pt atom, and a tip twice the size of a Pt atom. We also considered two limiting conditions for the relative contributions to the conduction band density of states. In the first, all atoms contribute equally, $D_W = D_O = D_{Na}$. In the second, we assume that the conduction band is formed by overlap of O $2p$ and W $5d$ orbitals and that Na $3s$ orbitals make only a weak contribution. Our numerical choices for the values of $D_i$ were guided by the results of Bullet's (39) calculation of the electronic structure of $NaWO_3$, which suggests that the contribution of the W orbitals to the conduction band is 10 times greater than that of the O orbitals ($D_O/D_W = 0.1$) and that the contribution of the O orbitals is 10 times greater than that of the Na orbitals ($D_O/D_{Na} = 10$).

## RESULTS AND DISCUSSION

Cleaved CTB surfaces were very rough on the submicrometer scale and areas with large flat terraces necessary for high resolution STM imaging were found only after tedious searches. The image in Fig. 1 shows one of the suitable areas that was occasionally encountered. The meandering terrace edges that separate the atomically flat

FIG. 1. 1000 × 1000 Å area of the cleaved CTB (001) surface showing a flat, terraced surface area. The vertical distance from black-to-white is 15 Å.

areas were characteristic for these samples, unlike the straight steps along high symmetry directions that we have observed on cleaved surfaces of other oxides (25). Annealing in vacuum at 500°C had no noticeable effect on the surface microstructure.

Images with atomic-scale features such as those shown in Fig. 2 have very small corrugations that are typically less than 1 Å. The highest resolution images show a periodic arrangement of round white (raised) features that have, within the accuracy of the piezo calibration, the periodicity of the unit cell. The two images shown in Fig. 2 are from two different samples. The first (a) is an "as cleaved" sample and the image in (b) is from a sample that was annealed. These images were chosen to represent

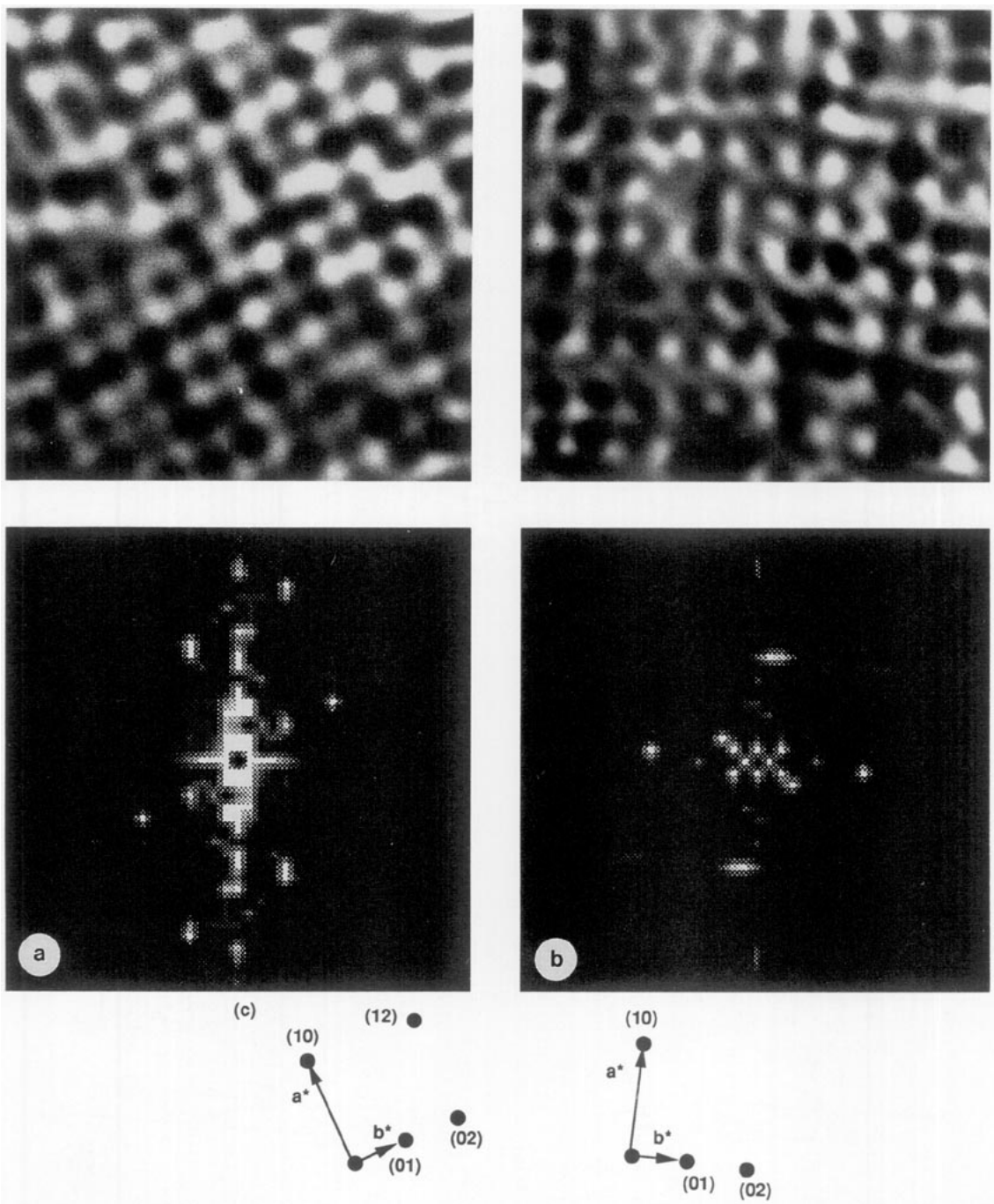


FIG. 2. Atomic-scale images of the cleaved CTB (001) surface. (a) 40 × 40 Å area, with 0.7 Å vertical distance from black-to-white. (b) 36 × 36 Å area, with 1.0 Å vertical distance from black-to-white. In both cases, two-dimensional Fourier transforms of the data are shown below. (c) Schematic indexing of the Fourier transforms.

the full range in variability of the atomic-scale observations. Because similar variations in the shape and appearance of the topographic features were observed on annealed and unannealed samples, we cannot attribute the differences to the thermal treatment. Possible explanations for the variations are local inhomogeneities in the Na distribution or differences in the detailed structure of the tip.

In spite of the variations, there are some features of the images that are always present. For example, all of the images appear to have a superperiodicity in at least one direction and in some cases, the periodicity seems to be doubled in both directions (see, for example, Fig. 2a). The existence of a superperiodic contrast variation is confirmed by the two-dimensional Fourier transforms (shown below the STM images) that have peaks corresponding to spatial frequencies that are twice the unit cell dimension. On the schematic representations in Fig. 2c, these peaks are labeled (01). Although the Fourier transforms of every observed image had a half-order spot corresponding to doubling of the periodicity in one direction, half-order spots in the second direction were either weak and diffuse or completely unobserved. Furthermore, the overwhelming majority of the images showed the $1 \times 2$ pattern, while only a few gave an indication of a $2 \times 2$ pattern (the image in 2a is the best example of these). Based on these data, we consider the best description for the surface repeat unit to be a rectangular $1 \times 2$ cell. Perpendicular domains of the $1 \times 2$ structure were observed on a single surface, but the boundary between domains was not imaged.

The observation of a $1 \times 2$ surface structure is consistent with the results of earlier low-energy electron diffraction experiments by other authors (12). Based on this diffraction data, surface cells with ordered arrangements of alkali have been proposed, but without specification of the termination layer or atomic relaxations. The details of the surface structure can be explored more completely based on a comparison of experimental STM observations and simulated images.

For the simulations, we consider two possible models that both have the stoichiometry of $Na_{3/4}WO_3$ and an ordered arrangement of sodium that doubles the size of the bulk unit cell in two directions, but the surface unit in only one. These are shown in Fig. 3 and are distinguished by the fact that model 1 has a Na–O terminated

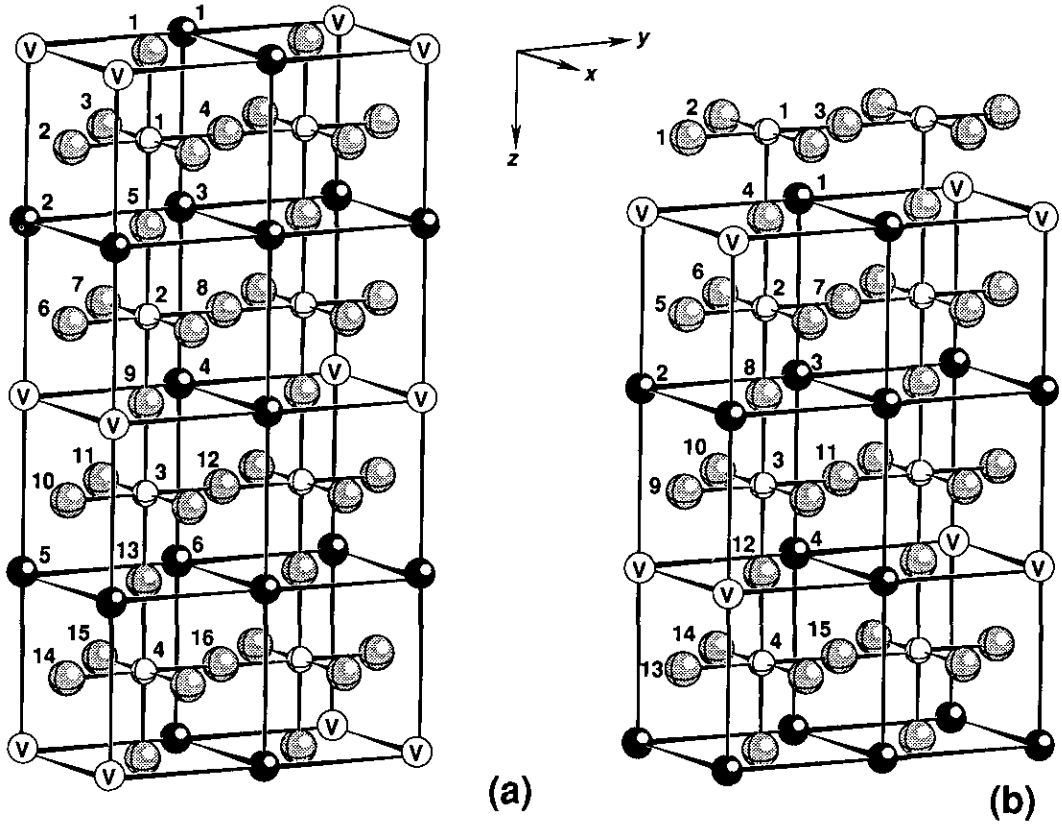


FIG. 3. Models used for the BV/DLS calculations. (a) The Na–O terminated surface. (b) The W–O terminated surface. The atoms at the lower edge of the models are fixed in their bulk positions and the free surface is at the top. The small gray spheres are the W atoms, the larger gray spheres are O atoms, and the black spheres are the Na atoms. The open circles with the V are Na vacancies. Numbering corresponds to the labels in Tables 2–5.

surface and model 2 has a W–O terminated surface. Although other structural models involving variations in the Na ordering scheme and termination layer were investigated, they did not yield the observed 1 × 2 pattern and were thus discounted.

The results of the crystal chemical calculations are summarized in Tables 2–5 and generally reflect the expected trends that are enforced by the empirical model. Specificially, the reduction in the coordination number of an atom on a surface or near a Na vacancy, in the absence of relaxation, decreases the bond valence sum at that atom. To satisfy the valence sum rule, the remaining bonds must shorten and strengthen to compensate for the missing bonds. The bond length changes induced by this compensation propagate through several coordination shells, diminishing as the distance from the defect increases. It should be noted that it is not always possible for the DLS simulation to position atoms in a configuration where the bond lengths and valence sums predicted by the BV calculation are fully realized because the surface area is constrained to the known value and atomic displacements are limited by point symmetry assignments. As a result, the valence at each atomic site (see Tables 3 and 5) does not always sum to the targeted value.

The shifts in atomic positions are summarized in Fig. 4. The relaxations on the W–O surface can be quantified by specifying the interlayer contraction and the surface rumpling which are 2% of the bulk spacing and 2% of the cubic lattice constant, respectively.The magnitude of these relaxations is rather small and thus the surface atoms do not achieve their expected valences. The valence on the surface W is only 84% of its bulk value and the surface oxygens are about 92% of their bulk values. This incomplete relaxation is a result of the constant surface area constraint; W–O bonds in the surface plane cannot contract without reducing the surface area. So, only limited valence compensation occurs through interlayer contraction and rumpling. The incomplete valence compensation should not be considered a failure of the

TABLE 2
Calculated Bond Lengths in the W–O Terminated Surface Model

| Contact | Multiplicity | Distance (Å) |
|---|---|---|
| W(1)–O(1) | 1 | 1.912 |
| W(1)–O(2) | 2 | 1.928 |
| W(1)–O(3) | 1 | 1.940 |
| W(1)–O(4) | 1 | 1.899 |
| W(2)–O(4) | 1 | 1.924 |
| W(2)–O(5) | 1 | 1.926 |
| W(2)–O(6) | 2 | 1.926 |
| W(2)–O(7) | 1 | 1.926 |
| W(2)–O(8) | 1 | 1.930 |
| W(3)–O(8) | 1 | 1.952 |
| W(3)–O(9) | 1 | 1.926 |
| W(3)–O(10) | 2 | 1.926 |
| W(3)–O(11) | 1 | 1.926 |
| W(3)–O(12) | 1 | 1.900 |
| W(4)–O(12) | 1 | 1.925 |
| W(4)–O(13) | 1 | 1.926 |
| W(4)–O(14) | 2 | 1.926 |
| W(4)–O(15) | 1 | 1.926 |
| W(4)–$O_{bulk}$ | 1 | 1.926 |
| Na(1)–O(2) | 2 | 2.740 |
| Na(1)–O(3) | 2 | 2.729 |
| Na(1)–O(4) | 4 | 2.720 |
| Na(1)–O(6) | 2 | 2.729 |
| Na(1)–O(7) | 2 | 2.727 |
| Na(2)–O(5) | 2 | 2.719 |
| Na(2)–O(6) | 2 | 2.733 |
| Na(2)–O(8) | 4 | 2.728 |
| Na(2)–O(9) | 2 | 2.702 |
| Na(2)–O(10) | 2 | 2.713 |
| Na(3)–O(6) | 2 | 2.725 |
| Na(3)–O(7) | 2 | 2.730 |
| Na(3)–O(8) | 4 | 2.719 |
| Na(3)–O(10) | 2 | 2.706 |
| Na(3)–O(11) | 2 | 2.710 |
| Na(4)–O(10) | 2 | 2.735 |
| Na(4)–O(11) | 2 | 2.743 |
| Na(4)–O(12) | 4 | 2.710 |
| Na(4)–O(14) | 2 | 2.714 |
| Na(4)–O(15) | 2 | 2.714 |

TABLE 3
Valence Sums in the W–O Terminated Surface Model

| Atom | Valence sum |
|---|---|
| W(1) | 4.94 |
| W(2) | 5.84 |
| W(3) | 5.85 |
| W(4) | 5.86 |
| Na(1) | 0.99 |
| Na(2) | 1.00 |
| Na(3) | 1.01 |
| Na(4) | 1.00 |
| O(1) | 2.03 |
| O(2) | 2.02 |
| O(3) | 2.04 |
| O(4) | 2.20 |
| O(5) | 2.12 |
| O(6) | 2.20 |
| O(7) | 2.28 |
| O(8) | 2.21 |
| O(9) | 2.12 |
| O(10) | 2.20 |
| O(11) | 2.28 |
| O(12) | 2.19 |
| O(13) | 2.12 |
| O(14) | 2.20 |
| O(15) | 2.28 |

TABLE 4
Calculated Bond Lengths in the Na–O Terminated Surface Model

| Contact | Multiplicity | Distance (Å) |
|---|---|---|
| W(1)–O(1) | 1 | 1.870 |
| W(1)–O(2) | 1 | 1.927 |
| W(1)–O(3) | 2 | 1.926 |
| W(1)–O(4) | 1 | 1.926 |
| W(1)–O(5) | 1 | 1.957 |
| W(2)–O(5) | 1 | 1.926 |
| W(2)–O(6) | 1 | 1.926 |
| W(2)–O(7) | 2 | 1.926 |
| W(2)–O(8) | 1 | 1.926 |
| W(2)–O(9) | 1 | 1.927 |
| W(3)–O(9) | 1 | 1.898 |
| W(3)–O(10) | 1 | 1.927 |
| W(3)–O(11) | 2 | 1.926 |
| W(3)–O(12) | 1 | 1.926 |
| W(3)–O(13) | 1 | 1.952 |
| W(4)–O(13) | 1 | 1.929 |
| W(4)–O(14) | 1 | 1.926 |
| W(4)–O(15) | 2 | 1.926 |
| W(4)–O(16) | 1 | 1.926 |
| W(4)–$O_{bulk}$ | 1 | 1.926 |
| Na(1)–O(1) | 4 | 2.547 |
| Na(1)–O(3) | 2 | 2.600 |
| Na(1)–O(4) | 2 | 2.605 |
| Na(2)–O(2) | 2 | 2.696 |
| Na(2)–O(3) | 2 | 2.714 |
| Na(2)–O(5) | 4 | 2.730 |
| Na(2)–O(6) | 2 | 2.722 |
| Na(2)–O(7) | 2 | 2.737 |
| Na(3)–O(3) | 2 | 2.704 |
| Na(3)–O(4) | 2 | 2.715 |
| Na(3)–O(5) | 4 | 2.718 |
| Na(3)–O(7) | 2 | 2.729 |
| Na(3)–O(8) | 2 | 2.729 |
| Na(4)–O(7) | 2 | 2.708 |
| Na(4)–O(8) | 2 | 2.712 |
| Na(4)–O(9) | 4 | 2.710 |
| Na(4)–O(11) | 2 | 2.735 |
| Na(4)–O(12) | 2 | 2.747 |
| Na(5)–O(10) | 2 | 2.694 |
| Na(5)–O(11) | 2 | 2.713 |
| Na(5)–O(13) | 4 | 2.729 |
| Na(5)–O(14) | 2 | 2.735 |
| Na(5)–O(15) | 2 | 2.735 |
| Na(6)–O(11) | 2 | 2.697 |
| Na(6)–O(12) | 2 | 2.702 |
| Na(6)–O(13) | 4 | 2.719 |
| Na(6)–O(15) | 2 | 2.733 |
| Na(6)–O(16) | 2 | 2.733 |

model since complete compensation would imply that atoms are as stable on the surface as in the bulk.

The relaxations on the Na–O terminated surface are considerably larger. In this case, because of the symmetry assignment, the O relaxations are not limited by the constant surface area constraint. It should also be noted that breaking the axial W–O bond reduces the valence sum at the surface O site by 50%. Thus, compensation is expected to be more dramatic. Again, the valence at the surface O is not entirely compensated (the sum is 1.4 instead of 2.2). Although a more complete compensation of this valence would be accomplished simply by the further shortening of the bond, it would lead to unrealistic interatomic separations. In the model described here, the interlayer spacing contracts by 12% and the surface rumpling is 4% of the cubic lattice constant.

Although it would be instructive to see if the results of these calculations are consistent with those of more established simulation techniques, we are unaware of any other calculations for the structure of this surface. However, both terminations of the (001) surface of the isostructural compound, $SrTiO_3$, have been studied using a computer simulation based on ionic pair-potentials (40). The results of that study predict surface rumpling similar in magnitude to what we have observed, 2 and 7% for the Ti–O and the Sr–O surfaces, respectively. The predicted interlayer contractions, however, differ significantly. While we find small relaxations, 2 and 12% for the W–O and Na–O, the ionic potential model predicts 22 and 24% for the Ti–O and the Sr–O surfaces, respectively. The

TABLE 5
Valence Sums in the Na–O Terminated Surface Model

| Atom | Valence sum |
|---|---|
| W(1) | 5.93 |
| W(2) | 5.83 |
| W(3) | 5.86 |
| W(4) | 5.85 |
| Na(1) | 1.00 |
| Na(2) | 1.00 |
| Na(3) | 1.01 |
| Na(4) | 1.01 |
| Na(5) | 1.00 |
| Na(6) | 1.01 |
| O(1) | 1.40 |
| O(2) | 2.13 |
| O(3) | 2.24 |
| O(4) | 2.35 |
| O(5) | 2.20 |
| O(6) | 2.12 |
| O(7) | 2.20 |
| O(8) | 2.29 |
| O(9) | 2.20 |
| O(10) | 2.12 |
| O(11) | 2.20 |
| O(12) | 2.28 |
| O(13) | 2.21 |
| O(14) | 2.11 |
| O(15) | 2.20 |
| O(16) | 2.28 |

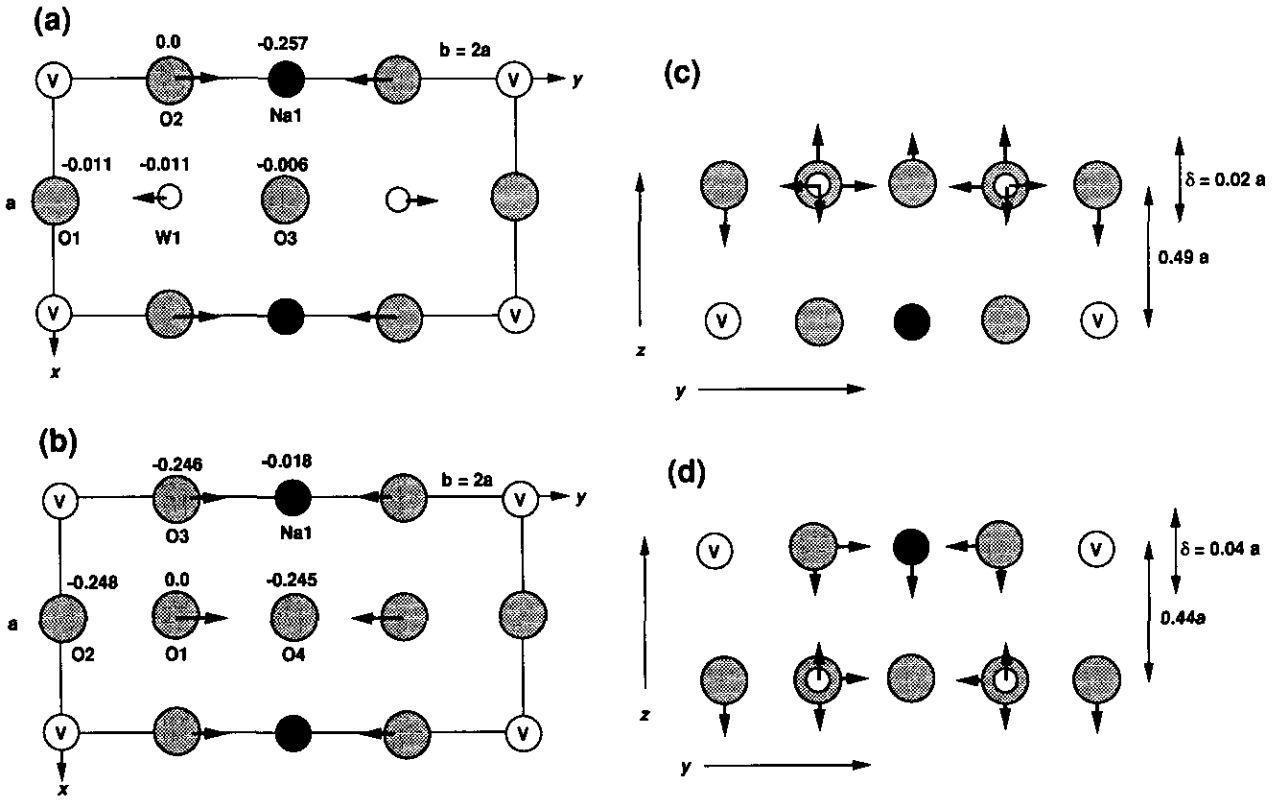


FIG. 4. Summary of the atomic relaxations. Arrows show the directions of the displacements from the ideal positions. (a) Projection down the $c$ axis of the W–O terminated surface, numbers above the atoms are fractional $c$ coordinates ($c = 2a$) assigning the highest atom to the 0 position. (b) The same representation for the Na–O surface. (c) & (d) are projections along [100] for the W–O terminated and Na–O terminated surfaces, respectively. The surface rumpling ($\Delta$) and the interlayer contraction are shown to the right. Numbering corresponds to the labels in Tables 2–5.

quantitative differences between the results of these two models are due at least in part to the dissimilarity of the perfect 2,4 modeled in the earlier work and the defective 1,5 perovskite considered here.

The fact that the crystal chemical model produces relaxations in expected directions and bond lengths within realistic limits leads us to believe that the predicted structures are a reasonable starting point for our image simulations, the results of which are presented in Fig. 5. Simulations of constant current images of the Na–O terminated surface are shown in Figs. 5a through 5f. Images (a–c) represent cases where all atoms contribute equally to the tunneling current and the size of the tip changes from a point (a), to a sphere with the radius of a single Pt atom (b), to a sphere with twice the radius of a Pt atom (c). The second three images (d–f) represent cases where the O atom's contribution to the tunneling current is 10 times greater than that of the Na atom, with the same increase in the tip size.

Note that in all cases, the apical O atom is the primary source of contrast and, because of its lateral relaxation toward the occupied Na site, a definite $1 \times 2$ structure is observed. Because the Na atom does not contribute significantly in images (d–f), the individual O atoms are more clearly differentiated. One particularly interesting effect is that the topographic peaks caused by the O atoms change position as the size of the tip changes. In Figs. 5a and 5d, the topographic peaks are exactly over the atoms, but as the tip size increases, contributions from neighboring atoms become increasingly important, so that the peak shifts to an intermediate position, apparently amplifying the actual atomic relaxations. This effect was consistently observed in all of the models and is undoubtedly the source of some of the variations in the experimental data. For example, lower resolution images showing only columns of atoms always had a stronger $1 \times 2$ character than the images that had high resolution in both scan directions. It should also be noted, however, that in all cases the topographic peak positions are closer together than those in the STM images, so these models of the Na–O surface do not account well for the observations.

Simulations of constant current images of the W–O terminated surface are shown in Figs. 5g–5l. Simulated images in (g–i) represent cases where all atoms contribute

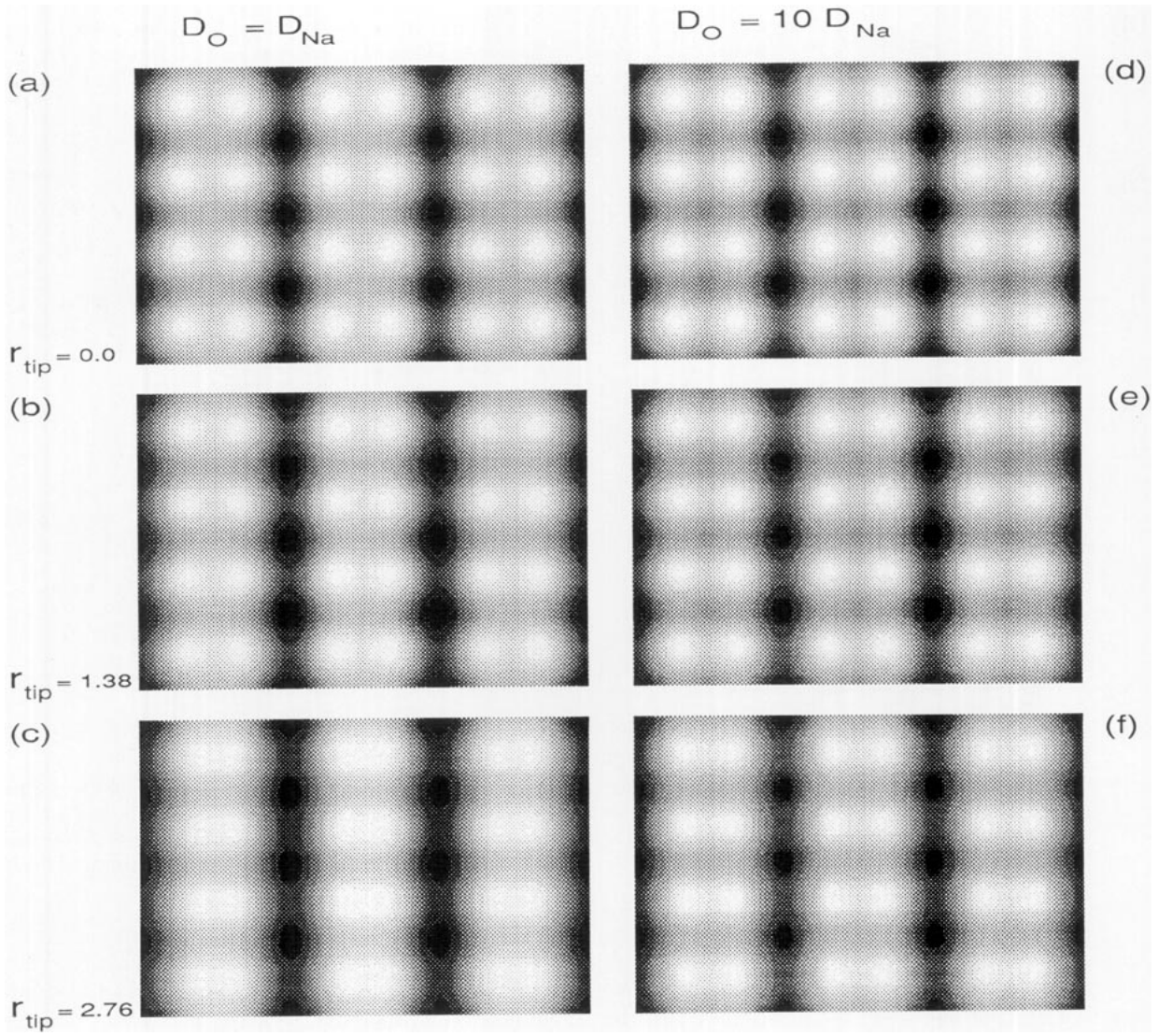


FIG. 5. Simulated constant current STM images. (a–c) Na–O, $D_O/D_{Na} = 1$; $r_{tip} = 0$, 1.38, 2.76, respectively. (d–f) Na–O, $D_O/D_{Na} = 10$; $r_{tip} = 0$, 1.38, 2.76, respectively. (g–i) W–O, $D_W/D_O = 1$; $r_{tip} = 0$, 1.38, 2.76, respectively. (j–l) W–O, $D_W/D_O = 10$; $r_{tip} = 0$, 1.38, 2.76, respectively.

equally to the tunneling current and the size of the tip increases in the manner described earlier. The second three images (j–k) represent the case where the W atom's contribution to the tunneling current is 10 times greater than that of the O atom, with the usual increments in tip size. The primary difference between these images is that in (g–i), where all atoms contribute equally to the tunneling current, the contrast is dominated by the surface O atoms and in the second three, it is dominated by the W atoms. As before, contrast variations in images formed with larger tips emphasize the surface relaxations that give the surface its 1 × 2 structure.

Based on the positions of the topographic peaks in the simulated constant current images, the simulation of the W–O terminated surface seems to most closely match the experimental observations. Furthermore, it is the model that assumes that the W atom makes a greater contribution to the tunneling current than the O atom and that the tip is the radius of one Pt atom that most closely matches the data. A comparison between this model and the image is shown in Fig. 6.

A recent STM study of the isostructural (001) surface of $SrTiO_3$ by Matsumoto *et al.* (24) also concluded that this surface was terminated by the analogous plane, Ti–O. However, this surface had a well-defined 2 × 2 surface structure that was probably related to the presence of surface O vacancies created during the 1200°C vacuum anneal to which the crystal was subjected. This should be

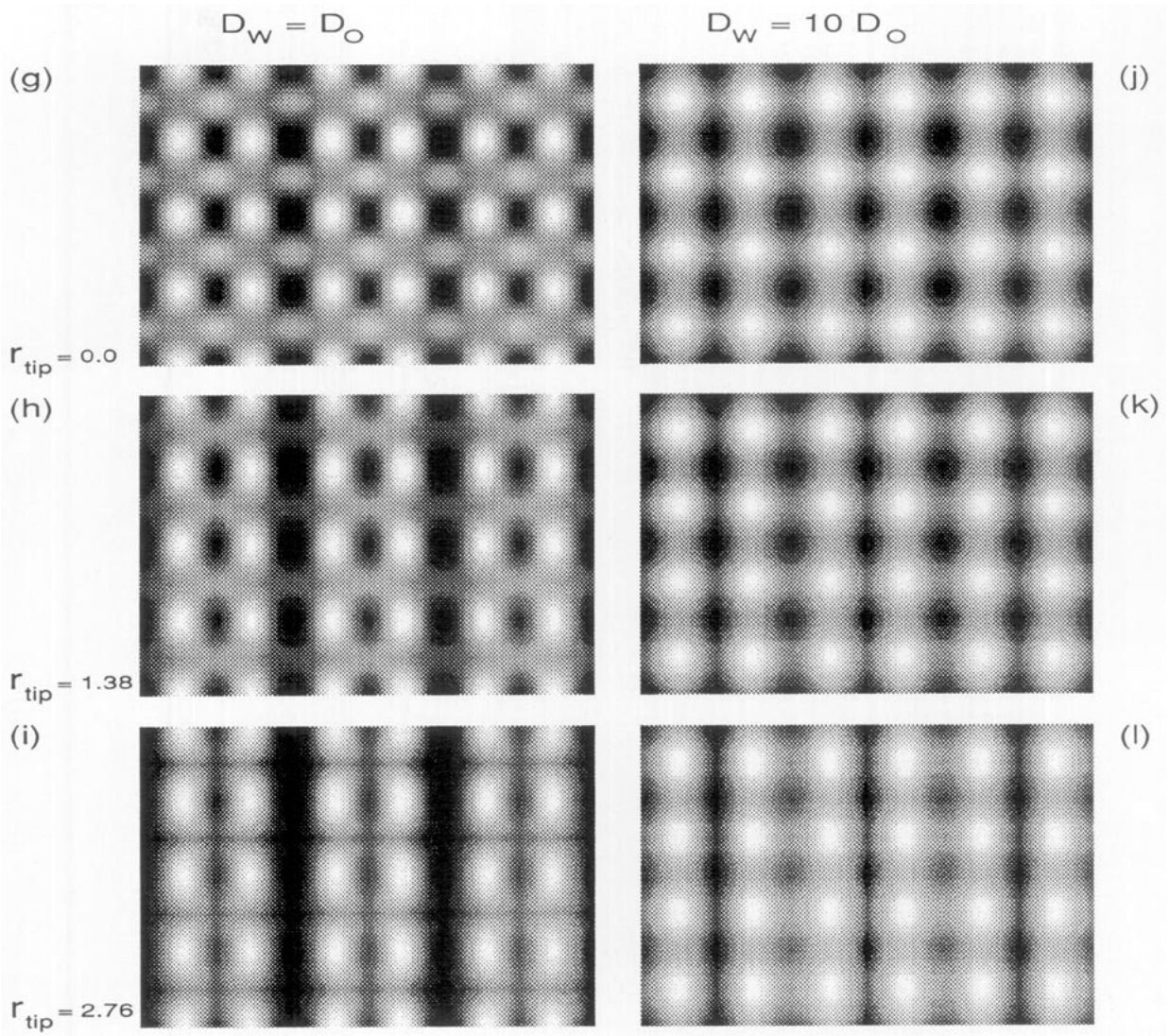


FIG. 5—*Continued*

contrasted with our cleaved surface that was intentionally imaged without annealing, to characterize the structure of a surface created mechanically at a low homologous temperature.

In an earlier study of the cleaved (0001) surface of a related hexagonal tungsten bronze, $Rb_{1/3}WO_3$, Lu *et al.* (25) observed two different termination layers. Such termination layer variations are an expected consequence of the cleavage process and our failure to observe the Na–O surface is unexpected. One possible explanation is that the actual differences in images of the Na–O and W–O terminated surfaces are more subtle than predicted by our simulations and, falling within the error of our observations, are not discriminated.

## CONCLUSION

Constant current STM images of cleaved (001) surfaces of the cubic tungsten bronze, $Na_{0.82}WO_3$, show atomic-scale contrast which has the periodicity of the bulk cell in one direction, but doubles in the other. A crystal chemical model predicts that if the sodium atoms order among their possible sites, atomic relaxations of the surface atoms would cause the observed super-periodic structure. Simulated constant current images of the W–O terminated surface are consistent with the observed images when it is assumed that the W atoms make a greater contribution to the tunneling current than the O atoms. We have found that structural modeling and image simulation not only

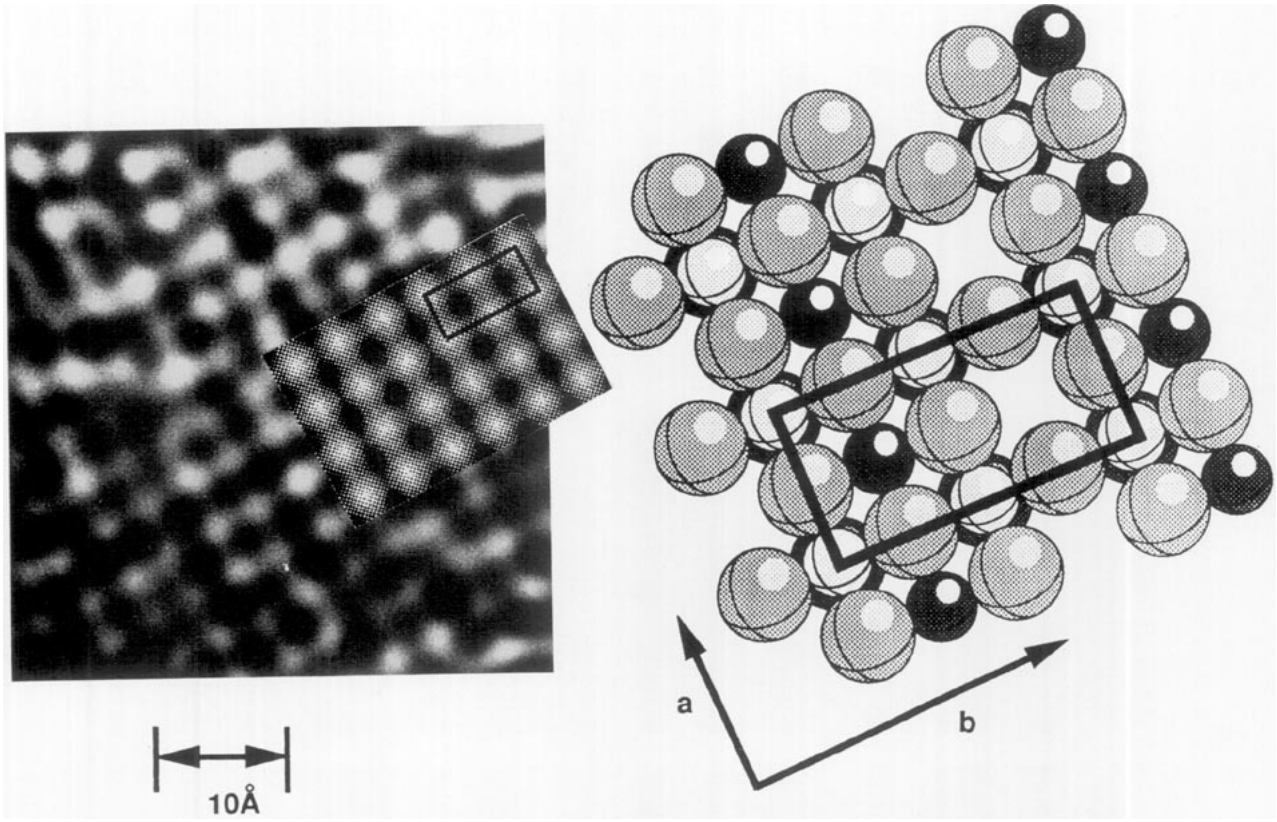


FIG. 6. STM image compared to an image simulation and atomic model for the CTB (001) 1 × 2 surface. The STM image is the same as the one shown in Fig. 2a. The inset is the simulated image of a W–O surface assuming that the tip has the radius of one Pt atom and that the W atoms make a greater contribution to the tunneling current than the O atoms.

provide a basis for surface structure assignment, but also provide insight into how contrast in the STM image is related to atomic positions and the way in which parameters such as tip size affect the appearance of the image.

## ACKNOWLEDGMENTS

This work was supported at Carnegie Mellon University by the National Science Foundation under Grant DMR-9107305 and under Grant CHE-9215173 at Marshall University.

## REFERENCES

1. A. S. Ribnick, B. Post, and E. Banks, *in* "Non-Stoichiometric Compounds" (R. F. Gould, Ed.), p. 246. Advances in Chemistry Series, American Chemical Society, 1963.
2. H. R. Shanks, P. H. Sidles, and G. C. Danielson, *in* "Non-Stoichiometric Compounds" (R. F. Gould, Ed.), p. 237. Advances in Chemistry Series, American Chemical Society, 1963.
3. L. D. Muhlestein and G. C. Danielson, *Phys. Rev.* **158,** 825 (1967).
4. L. D. Muhlestein and G. C. Danielson, *Phys. Rev.* **160,** 562 (1967).
5. T. Wolfram and L. Sutcu, *Phys. Rev. B* **31,** 7680 (1985).
6. H. R. Shanks, *Solid State Commun.* **15,** 753 (1974).
7. M. J. Sienko, *in* "Non-Stoichiometric Compounds" (R. F. Gould, Ed.), p. 224. Advances in Chemistry Series, American Chemical Society, 1963.
8. F. C. Zumsteg, *Phys. Rev. B* **14,** 1406 (1976).
9. P. G. Dickens and M. S. Whittingham, *Trans. Faraday Soc.* **61,** 1226 (1965).
10. N. Kosaka, Y. Sakai, and N. Tsuda, *J. Catal.* **98,** 95 (1986).
11. K. Machida, M. Enyo, G. Adachi, and J. Shiokawa, *J. Electrochem. Soc.* **135,** 1955 (1988).
12. M. A. Langell, S. L. Bernasek, *J. Vac. Sci. Technol.* **17,** 1287 (1980).
13. C. J. Schramm, M. A. Langell, and S. L. Bernasek, *Surf. Sci.* **110,** 217 (1981).
14. R. G. Egdell, H. Innes, and M. D. Hill, *Surf. Sci.* **149,** 33 (1985).
15. H. Nakamatsu, Y. Yamamoto, S. Kawai, K. Oura, and T. Hanawa, *Jpn. J. Appl. Phys.* **22,** L461 (1983).
16. J. N. Chazalviel, M. Campagna, G. K. Wertheim, and H. R. Shanks, *Phys. Rev. B* **16,** 697 (1977).
17. M. A. Langell and S. L. Bernasek, *Phys. Rev. B* **23,** 1584 (1981).
18. H. Hochst, R. D. Brigans, and H. R. Shanks, *Phys. Rev. B* **26,** 1702 (1982).
19. G. Hollinger, F. J. Himpsel, B. Reihl, P. Pertosa, and J. P. Doumerc, *Solid State Commun.* **44,** 1221 (1982).
20. R. G. Egdell and M. D. Hill, *Chem. Phys. Lett.* **85,** 140 (1982).
21. M. D. Hill and R. G. Egdell, *J. Phys. C: Solid State Phys.* **16,** 6205 (1983).
22. G. S. Rohrer, V. E. Henrich, and D. A. Bonnell, *Science* **250,** 1239 (1990).
23. R. Wiesendanger, I. V. Shvets, D. Bürgler, G. Tarrach, H. J. Güntherodt, J. M. D. Coey, and S. Gräser, *Science* **225,** 583 (1992).
24. T. Matsumoto, H. Tanaka, T. Kawai, and S. Kawai, *Surf. Sci. Lett.* **278,** L153 (1992).

25. W. Lu, N. Nevins, M. Norton, and G. S. Rohrer, *Surf. Sci. 291*, 395 (1993).
26. L. Pauling, *J. Am. Chem. Soc.* **51,** 1010 (1929).
27. I. D. Brown, *Phys. Chem. Miner.* **15,** 30 (1987).
28. M. O'Keeffe, *in* "Chemistry of Electronic Ceramic Materials" (P. K. Davies and R. S. Roth, Eds.), p. 485. NIST Special Publication 804, 1991.
29. I. D. Brown, *J. Solid State Chem.* **90,** 155 (1991).
30. I. D. Brown, *Solid State Ionics* **31,** 203 (1988).
31. M. O'Keeffe, *J. Mater. Res.* **6,** 2372 (1992).
32. H. R. Shanks, *J. Cryst. Growth* **13/14,** 433 (1972).
33. B. W. Brown and E. Banks, *J. Am. Chem. Soc.* **76,** 963 (1954).
34. I. D. Brown, *Acta. Crystallogr. Sect. B* **33,** 1305 (1977).
35. M. O'Keeffe, *Acta Crystallogr. Sect. A* **46,** 138 (1990).
36. I. D. Brown and D. Altermatt, *Acta Crystallogr. B* **41,** 244 (1985).
37. W. M. Meier and H. Villiger, Z. Kristallogr. **129,** 411 (1969).
38. W. H. Baur, *in* "Structure and Bonding in Crystals, Vol. 2." (M. O'Keeffe and A. Navrotsky, Eds.), p. 31. Academic Press, New York, 1981.
39. D. W. Bullett, *J. Phys. C: Solid State Phys.* **16,** 2197 (1983).
40. W. C. Mackrodt, *Phys. Chem. Miner.* **15,** 228 (1988).